Numerical Simulation of the Reactive Transport at Pore Scale in 3D

Vadim Lisitsa[1(✉)], Tatyana Khachkova[1], Dmitry Prokhorov[1], Yaroslav Bazaikin[1], and Yongfei Yang[2,3]

[1] Sobolev Institute of Mathematics SB RAS, 4 Koptug Avenue, Novosibirsk 630090, Russia
lisitsavv@ipgg.sbras.ru
[2] Key Laboratory of Unconventional Oil and Gas Development (China University of Petroleum (East China)), Ministry of Education, Qingdao 266580, People's Republic of China
[3] Research Center of Multiphase Flow in Porous Media, School of Petroleum Engineering, China University of Petroleum (East China), Qingdao 266580, People's Republic of China

Abstract. The paper presents a finite-difference algorithm for reactive transport simulation at the pore scale in 3D. We simulate the matrix dissolution and crystal precipitation due to heterogeneous reactions, acquired at the fluid-solid interface. The fluid flow and the reactive transport are computed using finite difference method on a regular rectangular mesh, whereas the immersed boundary conditions are applied to account for irregular interface geometry. The time-evolving pore-to-matrix surface is defined implicitly by the level-set method. The algorithm is implemented using Graphic Processor Units.

Keywords: Pore-scale · Reactive transport · Level-set · Immersed boundaries

1 Introduction

There are numerous application of the reactive transport simulation, such as enhanced oil recovery [7], CO_2 sequestration in carbonate formations [17], biocementation [5], salt precipitation [3], and injection of non-condensable gases into geothermal fields [11]. At the pore scale, the main mechanism causing changes in the pore space geometry and morphology is the heterogeneous reactions at the fluid-solid interface. These reactions may lead to matrix dissolution or minerals precipitation. Changes in the pore space and rock matrix structure at the pore scale affect the macroscopic properties of the rocks, including porosity, hydraulic permeability [2,15], mechanical compliance [13], electric resistivity [12] and others.

The research was supported by the Russian Science Foundation grant no. 21-71-20003.

© Springer Nature Switzerland AG 2021
O. Gervasi et al. (Eds.): ICCSA 2021, LNCS 12958, pp. 375–387, 2021.
https://doi.org/10.1007/978-3-030-87016-4_28

Nowadays, predictive reactive transport simulations are used to estimate the effect of chemically active fluid filtration at the reservoir scale in application to CO_2 sequestration geothermal fields exploration and others [23]. At the reservoir scale, permeability, diffusion coefficient, reaction rates, and species concentrations are defined inside the grid cells and connected to the porosity be some empirical relations. These relations came from the lab [13] or using analytical averaging techniques for relatively simple structures [4]. In the lab, it is generally troublesome to reproduce the reservoir conditions (pressure, temperature, etc.). Moreover, the experiments are time-consuming, and they can be conducted only once for a single sample. The analytical averaging applies to relatively simple models, such as a periodical, and they are hard to extend to real rocks or porous materials structure. Thus, numerical simulation is the most attractive option because it combines lab experiments' flexibility with theoretical investigations' accuracy. Moreover, it is possible to vary input parameters such as inlet pressure of flow rate, reactions rates, etc., and estimate their effect on the macroscopic parameters used in the reactive transport models at the reservoir scale; see [23] for a review.

Transport at the pore-scale fluid flow has to be simulated directly by solving Stokes or Navier-Stokes equation. Then the solution of the convection-diffusion equation provides the distribution of the active components. Finally, the evolution of the fluid-solid interface has to be simulated [18]. The main difference in the known approaches to simulate reactive transport at the pore scale is the interface treatment. The simplest approach is to use the same regular mesh to approximate Stokes and convection diffusion equation and to define a formal parameter such as mass or volumetric fraction of the solid phase in the "boundary" cells. After that additional equations are introduced to estimate changes of the introduced parameter due to chemical reactions [10,26]. This approach is easy to implement, however it requires the additional equation are based on a number of empirical relations. Among the methods based on the direct representation of the interface and heterogeneous reactions, it is worth mentioning the front-tracing, level-set, and phase-field methods. In the front-tracking method, the interface is represented explicitly and then combined with the finite-volumes and truncated-cell approach to simulate fluid flow and reactant transport [18]. However, this approach is hard to implement in domains with complex topology and geometry, which is always the case for porous materials. Implicit representation of the interface used in the level-set [19], and phase-field [25] methods, where the interface is the zero-level of an arbitrary function. This representation simplifies the treatment of the interface evolution, including the topology changes. Moreover, the last two methods are implemented on the regular rectangular meshes in combination with the immersed boundary method [20,22] for the level-set, or the diffused interface approach for the phase-field.

In this research, we developed the level-set based algorithm for the reactive transport simulation at the pore scale. We state the problem and formulate the mathematical model in Sect. 2. In Sect. 3 we provide numerical algorithms to solve Stocks, equation, convection-diffusion equation, and level-set evolution

and redistancing. We illustrate applicability of the algorithm to simulation of the pore space geometry changes in a carbonate rock due to chemical dissolution in Sect. 4.

2 Statement of the Problem

We assume that the interface moves with the slowest rate to simulate reactive transport at the pore scale. Thus, this rate defines the time scale of the problem in general. The fluid flow rate is also low, and it stabilizes instantly when pore space geometry changes slightly. Thus, the problem can be split into three stages: solution of Stokes equation to define the flow in the pore space, solution of the convection-diffusion equation to simulate the chemical species propagation, and correction of the pore space geometry due to dissolution.

We consider the problem stated in $D \subseteq R^3$. The domain is bounded. Assume, that $D = D_p(t) \cup D_m(t)$, where $D_p(t)$ and $D_m(t)$ correspond to pore space and the rock matrix, respectively. Subdomains $D_p(t)$ and $D_m(t)$ are time-dependent and nonintersecting. We define the domain boundary as $\partial D = S_{outlet} \cup S_{inlet} \cup S_{nf}$, where S_{outlet} and S_{inlet} are the outlet and inlet surfaces, S_{nf} correspond to all other boundaries where the no-flow boundary condition will be used. We also introduce the pore-to-matrix interface as $\bar{D}_p(t) \cap \bar{D}_m(t) = S(t)$. A sketch of the model is presented in Fig. 1.

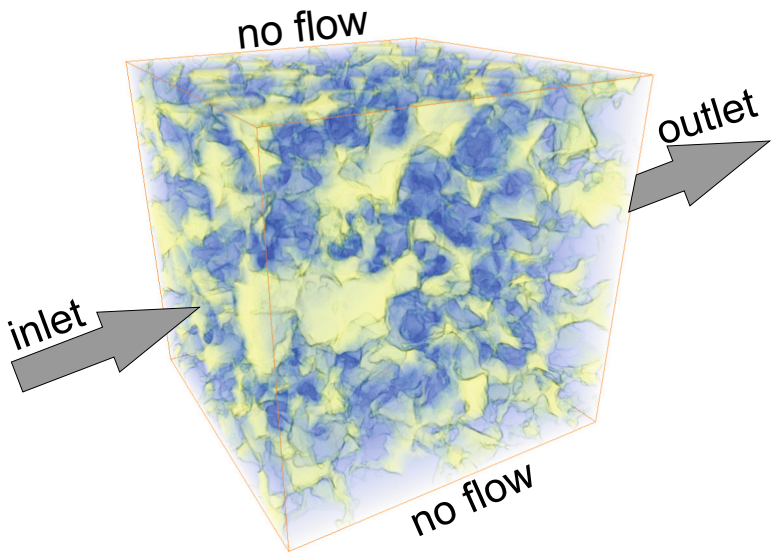

Fig. 1. A sketch of the computational domain. The matrix of the material is blue, the pore space is green. (Color figure online)

The fluid flow is simulated in the pore space $D_p(t)$ by solving steady-state Stokes equation:

$$\begin{aligned} &\mu\nabla^2\boldsymbol{u} - \nabla p = 0, \\ &\nabla \cdot \boldsymbol{u} = 0. \end{aligned} \tag{1}$$

with boundary conditions

$$\begin{aligned} &\boldsymbol{u}(\boldsymbol{x}) = 0, \qquad \boldsymbol{x} \in S(t) \cup S_{nf}, \\ &p(\boldsymbol{x}) = p_{bc}(\boldsymbol{x}), \, \boldsymbol{x} \in S_{inlet} \cup S_{outlet}, \end{aligned} \tag{2}$$

where p is the fluid pressure, $\boldsymbol{u} = (u_1, u_2, u_3)^T \in R^3$ is the velocity vector, μ is the dynamic viscosity of the fluid, $p_{bc}(\boldsymbol{x})$ are the values of the pressure at the opposite boundaries S_{inlet} and S_{outlet}, the spatial coordinates are defined by the vector $\boldsymbol{x} = (x_1, x_2, x_3)^T$.

Propagation of the reactant in $D_p(t)$ satisfies the convection-diffusion equation:

$$\frac{\partial C}{\partial t} + \nabla \cdot (\boldsymbol{u}C - D\nabla C) = 0, \tag{3}$$

with boundary conditions:

$$\begin{aligned} &D\tfrac{\partial C}{\partial \boldsymbol{n}} = k_r(C - C_s), \, \boldsymbol{x} \in S(t), \\ &C = C_{in}, \qquad\qquad\quad \boldsymbol{x} \in S_{inlet}, \\ &\tfrac{\partial C}{\partial \boldsymbol{n}} = 0, \qquad\qquad\quad \boldsymbol{x} \in S_{outlet} \cup S_{nf}. \end{aligned} \tag{4}$$

In these notations, the diffusion coefficient is D, C is the active component concentration, vector of the inner normal is $\boldsymbol{n}$, k_r is the reaction rate. We assume the heterogeneous reactions are much slower, than homogeneous ones. Thus, we omit right-had sides in Eq. (3).

Chemical reaction of the first-order causes the changes in the interface, which are governed by the following equation:

$$v_n(\boldsymbol{x}, t) = \tfrac{K_c k_r}{\rho}(C - C_s), \, \boldsymbol{x} \in S(t), \tag{5}$$

where v_n is the normal component of the interface velocity, K_c is the stoichiometric coefficient, k_r is the reaction rate (4), ρ is the mass density of the matrix mineral, C_s is equilibrium concentration of the reactant.

2.1 Implicit Definition of the Interface

To define the interface implicitly we use the level-set method [19]. It means, that we introduce an artificial function $\varphi(\boldsymbol{x}, t)$, so that the interface $S(t)$ is the zero-level of function $\varphi(\boldsymbol{x}, t)$; i.e.

$$S(t) = \{\boldsymbol{x} | \varphi(\boldsymbol{x}) = 0\}.$$

Consequently, we define subdomains D_p and D_m as

$$D_p(\boldsymbol{x}, t) = \{\boldsymbol{x} | \varphi(x, t) > 0\}, \, D_m(\boldsymbol{x}, t) = \{\boldsymbol{x} | \varphi(x, t) < 0\}.$$

Typically, the level-set function is the signed-distance from the interface. Thus, $\|\nabla_x \varphi(\boldsymbol{x}, t)\| = 1$, and

$$\boldsymbol{n} = \nabla_x \varphi(\boldsymbol{x}, t).$$

The interface evolution Eq. (5) can be extended to the level-set function as follows [8,19]:

$$\begin{array}{l} \frac{\partial \varphi(\boldsymbol{x},t)}{\partial t} + v_n(\boldsymbol{x}, t) = 0, \\ \varphi(\boldsymbol{x}, 0) = \varphi_0, \end{array} \tag{6}$$

where v_n is the normal velocity, as defined by Eq. (5).

3 Finite-Difference Approximation

To solve Eqs. (1), (3), and (6) numerically, we suggest applying the finite-differences. In particular, the staggered-grid schemes will be used. Introduce a regular rectangular grid with the grid cells $C_{i,j,k} = [h_1(i-1/2), h_1(i+1/2)] \times [h_2(j-1/2), h_2(j+1/2)] \times [h_3(k-1/2), h_3(k+1/2)]$ and define the pressure, concentration, and the level-set function in the centers of the cells $p_{i,j,k} = p(ih_1, jh_2, kh_3)$, $C^n_{i,j,k} = C(ih_1, jh_2, kh_3 n\tau)$, and $\varphi^n_{i,j,k} = \varphi(ih_1, jh_2, kh_3, n\tau)$, velocity components are placed at the corresponding faces $(u_1)_{i+1/2,j,k} = u_1((i+1/2)h_1, jh_2, kh_3)$, $(u_2)_{i,j+1/2,k} = u_2(ih_1, (j+1/2)h_2, kh_3)$, $(u_3)_{i,j,k+1/2} = u_3(ih_1, jh_2, (k+1/2)h_3)$. In these notations h_1, h_2, and h_3 are the grid steps in space, τ is the grid step in time.

3.1 Approximation of Stokes Equation

We use the second-order accurate finite-difference scheme to approximate Eq. 1:

$$\begin{array}{ll} \mu L[u_1]_{i+1/2,j,k} - D^c_1[p]_{i+1/2,j,k} = 0, & \text{if } \varphi_{i+1/2,j,k} > 0, \\ \mu L[u_2]_{i,j+1/2,k} - D^c_2[p]_{i,j+1/2,} = 0, & \text{if } \varphi_{i,j+1/2,k} > 0, \\ \mu L[u_3]_{i,j,k+1/2} - D^c_3[p]_{i,j,k+1/2} = 0, & \text{if } \varphi_{i,j,k+1/2} > 0, \\ D^c_1[u_1]_{i,j,k} + D^c_2[u_2]_{i,j,k} + D^c_3[u_3]_{i,j,k} = 0, & \text{if } \varphi_{i,j,k} > 0, \end{array} \tag{7}$$

where

$$L[f]_{I,J,K} = D^2_1[f]_{I,J,K} + D^2_2[f]_{I,J,K} + D^2_3[f]_{I,J,K} \tag{8}$$

$$D^2_1[f]_{I,J,K} = \frac{f_{I+1,J,K} - 2f_{I,J,K} + f_{I,J,K}}{h_1^2} = \left.\frac{\partial^2 f}{\partial x_1^2}\right|_{I,J,K} + O(h_1^2), \tag{9}$$

$$D^c_1[f]_{I,J,K} = \frac{f_{I+1/1,J,K} - f_{I,J-1/2,K}}{h_1} = \left.\frac{\partial f}{\partial x_1}\right|_{I,J,K} + O(h_1^2). \tag{10}$$

Indices I, J, and K can be integer or fractional, but i, j, and k are integers only. The operators approximating derivatives with respect to the other spatial direction can be obtained by the permutations of the role of spatial indices. Note, that the projection-type methods to solve Stokes equation are based on the solution of the Poisson equation to correct the pressure. This equation is stated with Neumann boundary conditions at the interface Γ and appropriate boundary

conditions at the inlet and outlet boundary. Thus the problem is equivalent to numerical simulation of electric current in pore space, and can be efficiently solved with Krylov-type methods with suitable preconditioner [12].

The level-set function defines the interface which is not aligned to the grid lines, thus immersed boundary conditions (IBC) are required to treat the boundary conditions properly [9,14,16]. The idea of the IBC is to extrapolate the solution to the points belonged to $D_m(t)$ which are close to the interface and required for the computation. After that the solution can be computed using (7) in all points inside the domain $D_p(t)$.

3.2 Approximation of the Convection-Diffusion Equation

To approximate Eq. (3) We use the first-order accurate scheme:

$$\begin{gathered}\frac{C^{n+1}_{i,j,k}-C^{n}_{i,j,k}}{\tau}+D^1_1[u_1C]^n_{i,j,k}+D^1_2[u_2C]^n_{i,j,k}+D^1_3[u_3C]^n_{i,j,k}-DL[C]^n_{i,j,k}=0,\\ \varphi_{i,j,k}>0,\end{gathered} \tag{11}$$

where

$$\begin{gathered}D^1_1[u_1C]^n_{i,j,k}=\frac{F_{i+1/2,j,k}-F_{i_1-1/2,j,k}}{h},\\ F_{i+1/2,j,k}=\begin{cases}(u_1)_{i+1/2,j,k}C_{i+1,j,k}, & (u_1)_{i+1/2,j,k}<0\\ (u_1)_{i+1/2,j,k}C_{i,j,k}, & (u_1)_{i+1/2,j,k}>0\end{cases}\end{gathered} \tag{12}$$

Operators, approximating the derivatives to the other spatial direction, can be obtained using the spatial indices' permutation. Operator $D[f]_{I,J,K}$ is introduced above in Eq. (8).

Similar to the Stokes equation approximation, we use the IBC to account for the Robin boundary condition at the interface $S(t)$. Detailed discussion of IBC construction for the Robin boundary conditions in reactive transport is presented in [15].

3.3 Interface Evolution

Evolution of the interface satisfy Eq. (6), which can be solved by finite differences:

$$\frac{\varphi^{n+1}_{i,j,k}-\varphi^{n}_{i,j,k}}{\tau}=-(v_n)^n_{i,j,k}, \tag{13}$$

where $(v_n)^n_{i,j,k}$ is the velocity of the surface.

Function $\phi(\boldsymbol{x}),t$ is defined in the entire domain D, and the Eq. (6) is also should be satisfied in D. However, its the right-hand side (function $v_n(\boldsymbol{x})$) is defined only at the interface S, thus, it needs to be prolongated elsewhere. It can be done, by assuming $v_n(\boldsymbol{x})$ is constant along the normal direction to S. Thus, v_n is the steady-state solution of the following equation:

$$\begin{gathered}\frac{\partial q}{\partial t}+sign(\varphi)\left(\frac{\nabla\varphi}{|\nabla\varphi|}\cdot\nabla q\right)=0,\\ q(\boldsymbol{x},0)=\tilde{v}_n(\boldsymbol{x},t_0),\end{gathered} \tag{14}$$

where $\tilde{v}_n$ are the initial conditions, that is the velocity at the interface.

Following [6] we approximate gradient of φ with central-difference scheme, and apply the upwind scheme to compute the spatial derivatives of q. The solution of (14) is only required inside a strip $D_s = \{\boldsymbol{x} : |\varphi(\boldsymbol{x})| \leq 2\sqrt{h_1^2 + h_2^2 + h_3^2}\}$. This means, that the solution can be obtained in as few as 3–5 iterations. Also, a redistancing procedure is needed to keep the φ being a signed distance [24].

4 Numerical Experiments

4.1 Validation Against Lab Data

To illustrate the algorithm's applicability to the realistic models, we considered the CT-scans of an aquifer in the Middle East carbonate samples presented in [2]. Four different samples were studied in [2] subjected to CO_2 saturation with the further dissolution of the carbonate matrix. The samples' difference was in the original pore space structure and the flow rate used for the saturation. Ten CT-scans were acquired during the saturation process for each sample to follow the pore space evolution. The CT-scans are provided in [1]. We considered the sample called AH from the set. We subtract a subvolume of 200^3 voxels to simulate the reactive transport in the carbonate. The CT-scans resolution was 5.2 μm per voxel; thus, the considered subsamples' size was about one mm^3.

We consider the solid matrix and the fluid properties according to [2]. The core matrix is calcite with mass density $\rho = 2710$ kg/m^3, and stoichiometric coefficient of the reaction equals to one; i.e., $K = 1$. The fluid is the reservoir water under the assumption that changes in the reactant concentration do not affect the fluid's physical properties. Thus we fix the dynamic viscosity $\mu = 0.00028$ Pa·s. The diffusion coefficient was equal to $7.5 \cdot 10^{-9}$ m^2/s, reaction rate $k_r = 0.08$ m/s, and the pressure drop was 4 Pa. The active component is the cation H^+ with equilibrium concentration corresponding to $pH = 7$, whereas acidity at the inlet was $pH = 3$ following laboratory experiments presented in [13].

In Fig. 2 we provide the pore space and the flow stream-lines at three different time instants. It is noticeable that the main flow path is formed, causing the wormhole creation. To illustrate the influence of the pore space changes on the rock's hydro-dynamical properties, we provide the plots of the porosity, permeability, and tortuosity as functions of model time (Fig. 3). Both porosity and permeability increase in time, but relatively low porosity increase leads to the substantial increase of permeability due to the wormholes formation. At the same time, tortuosity decreases slightly because the preferred flow path preexisted in the original model (the top picture in Fig. 2). The cross-plots of permeability in dependence on porosity and tortuosity in dependence on porosity are provided in Fig. (4), showing a rapid increase of the permeability when porosity increases. These results are in the agreement with lab measurements provided in [2].

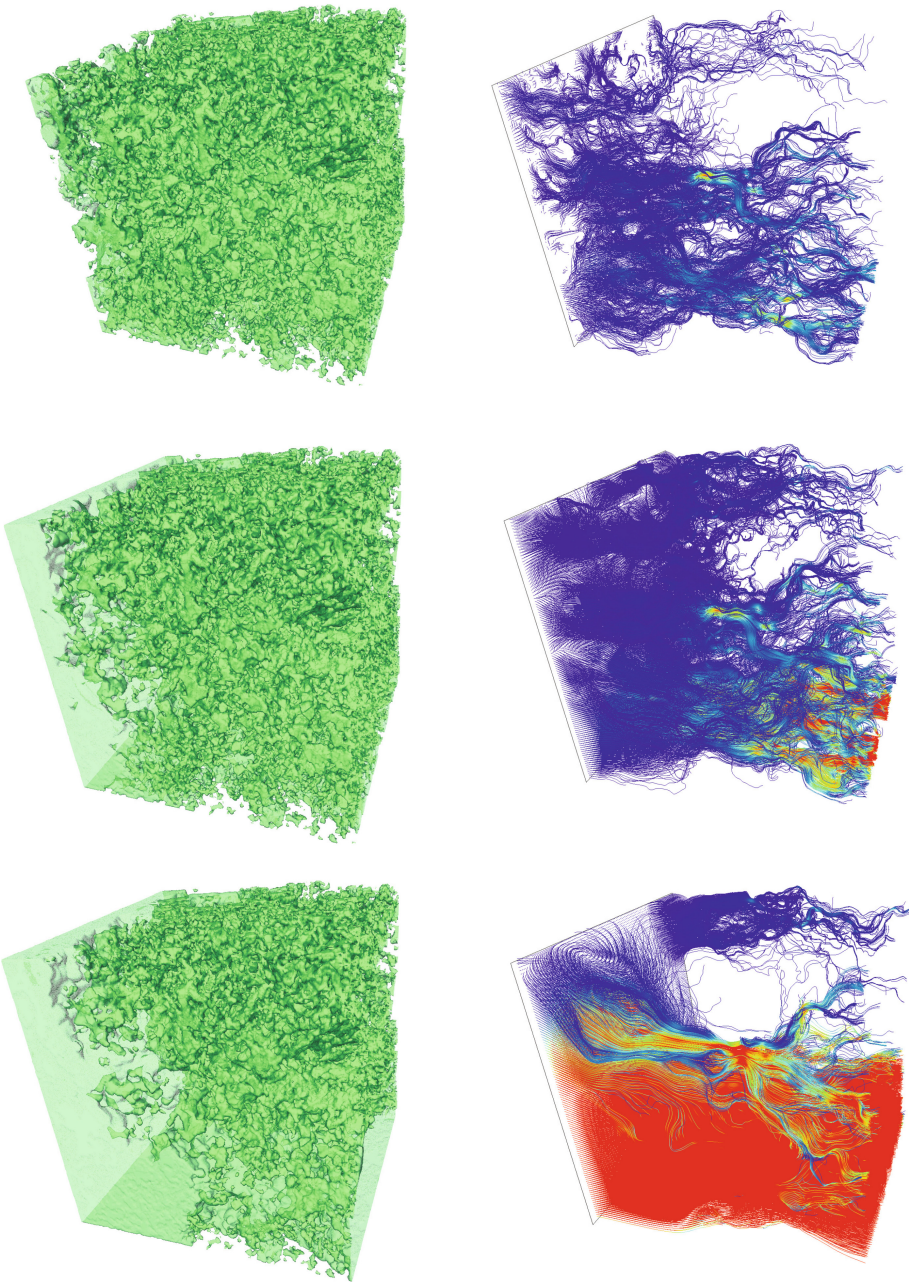

Fig. 2. Pore space representation (left) and stream-lines (right) at different time instants (0, 500, 1000 s.) for the simulation of carbonate dissolution.

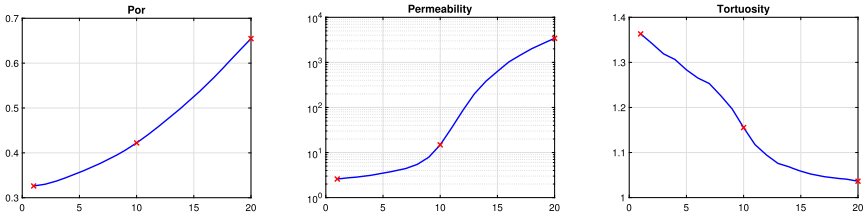

Fig. 3. Dependence of the porosity (left), permeability (middle), and trotuosity (right) on the model time. Red markers correspond to instants from Fig. 2. (Color figure online)

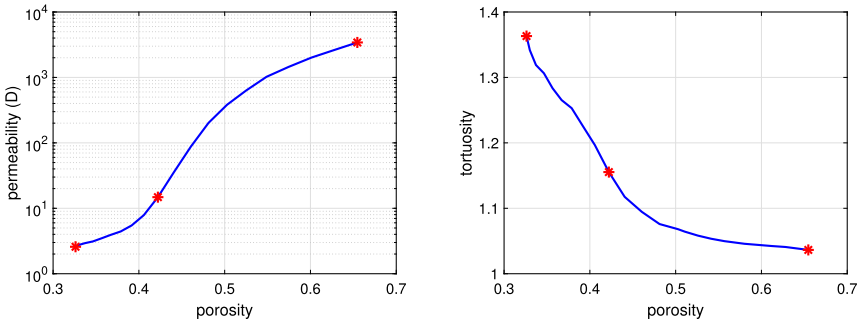

Fig. 4. Cross-plots of permeability in dependence on porosity (left) and tortuosity in dependence on porosity (right). Red markers correspond to instants from Fig. 2. (Color figure online)

4.2 Analysis of the Topology Changes Due to Chemical Matrix Dissolution

In the previous experiment we illustrated that the reaction rate k_{chem}, diffusion coefficient D, flow rate defined by the pressure drop dP, and initial species concentration defined by pH strongly affect the changes in the geometry and topology of the pore space, as well as permeability of the rock sample. To study these effects we performed a series of simulations varying the parameters as follows: $k_{chem} \in \{10^{-3}, 10^{-2}, 10^{-1}, 10^{0}\}$, $D \in \{10^{-9}, 10^{-8}, 10^{-7}\}$, $dP \in \{0.5, 1, 2\}$, $pH \in \{3, 4, 5\}$. As the pore space model we considered the same CT-scan as before. We simulated reactive transport up to 1000 s of the model time, fixing the level-sets every 10 s. Thus, we get a series of 100 pore space geometries for each simulations. Also, we estimated the changes in the permeability, hydraulic tortuosity, and formation factors at the same time instants. Later, using the saved level-sets we estimated the porosity and specific surface of the pore space as function of time. Moreover, we compute the persistence diagrams for one-dimensional Betti number, that is the topological parameters of the pore space indicating the number of independent cycles (channels) [21]. We assume that the changes in pore space topology may characterize the evolution of the hydraulic permeability of the sample. Similar to what was done in 2D case in [15], we intro-

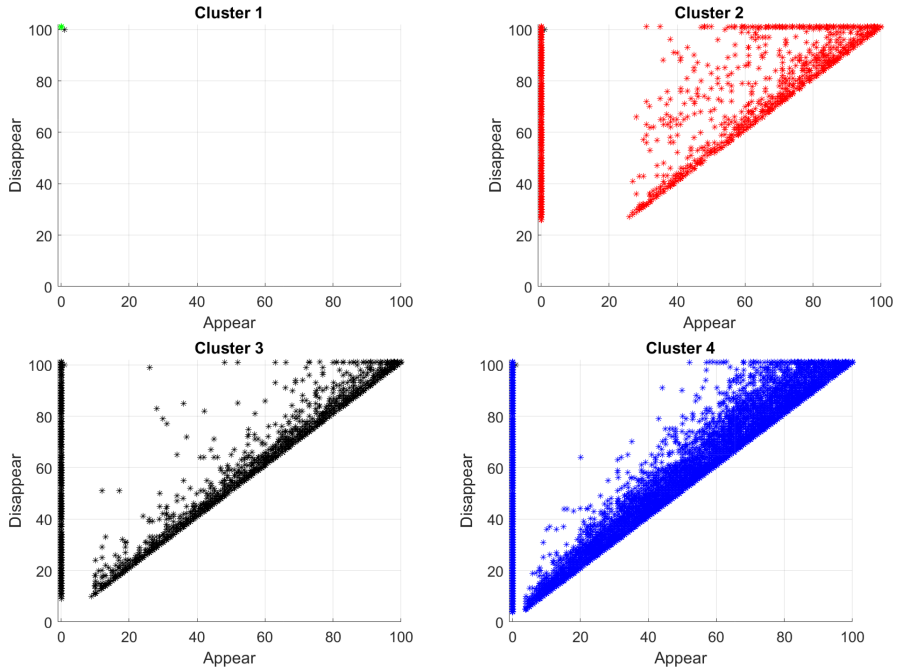

Fig. 5. Persistence diagrams for Betti 1 number of the pore space topology. Horizontal axis indicate the instant when a new component appears. Vertical one represents the instant when a component disappears.

duced the formal measure in the space of the persistence diagrams and applied K-means clustering procedure to separate different scenarios of pore space topology evolution. We stable got four different clusters, with persistence diagrams for mean element in each cluster presented in Fig. 5. According to the diagrams the models from the first cluster remain unchanged, because all connectivity components exist up to the very last instant. The topology of the samples from the three clusters evolved significantly, with the intensity of the pore space changes increases with the cluster number. This assumption is also confirmed by the porosity and permeability changes (Fig. 6). Both porosity and permeability of the models from the blue cluster grow rapidly, whereas they remain constant for the models from the green cluster. Finally, we considered how the separation into clusters related to the input parameters. In Fig. 7 we provide the correspondence between the input parameters dP, D, k_{chem} and the clustering with respect to persistence diagrams, where the positions of the points correspond to the coordinates in the space of the input parameters, and the colors correspond to the different clusters. Note, that the dominating parameter is the reaction rate. Moreover if the reaction rate is low, the results are independent of dP, D; indeed no reaction accrues in this case. However, if the reaction takes

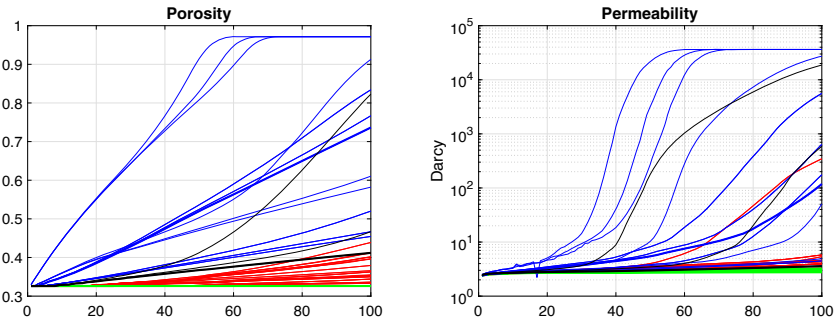

Fig. 6. Evolution of the porosity (left) and permeability (right). Different colors correspond to different clusters. (Color figure online)

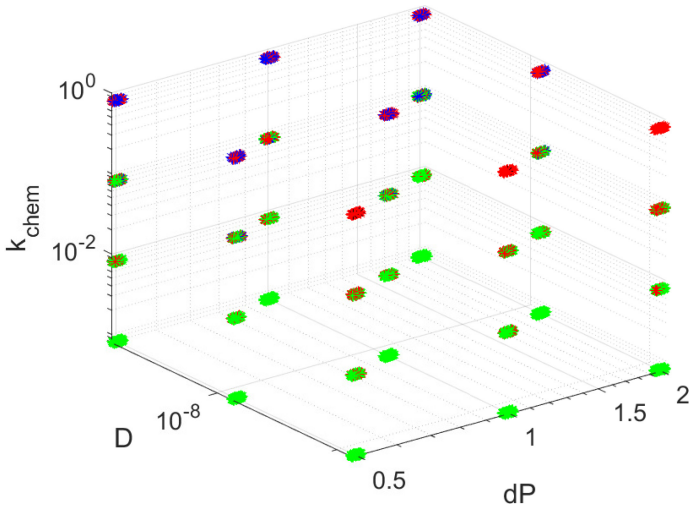

Fig. 7. Correspondence between the input parameters dP, D, k_{chem} and the clustering with respect to persistence diagrams. The positions of the points correspond to the coordinates in the space of the input parameters, and the colors correspond to the different clusters. (Color figure online)

place ($k_{chem} > 10^{-2}$) the changes in the pore space topology are affected by the diffusion, rather than the flow rate.

5 Conclusions

We presented an algorithm for numerical simulation of reactive transport at the pore scale in 3D. The algorithm is based on the combination of the level-set method to handle evolution of the pore-to-matrix interface with finite differences to simulate fluid flow and reactive transport. Implementation of the algorithm

is oriented on the use of GPUs; i.e., all numerical simulations are performed using GPUs. In the current research we presented the results computed using a single-GPU implementation which allows us simulating reactive transport in models of the size of up to 300^3 voxels. However, the algorithm is easy to extend to multi-GPU architecture. To illustrate applicability of the algorithm to a realistic problems we simulated $C0_2$ injection to a carbonate sample. Moreover, we performed a series of simulations varying input parameters such as reaction rate, flow rate and the diffusion coefficient and studied their effect on the pore space topology changes. In particular, we suggested a new methodology to quantify the changes in the topology based on the persistence diagrams for one dimensional Betti numbers. The use of the bottleneck metric in the space of the persistence diagrams allowed us to apply clustering techniques, to distinguish different scenarios of core matrix dissolution.

Simulation were performed using computational resources of Peter the Great Saint-Petersburg Polytechnic University Supercomputing Center (https://www.spbstu.ru/).

References

1. Al-Khulaifi, Y., Lin, Q., Blunt, M., Bijeljic, B.: Pore-scale dissolution by CO_2 saturated brine in a multi-mineral carbonate at reservoir conditions: impact of physical and chemical heterogeneity (2019). https://doi.org/10.5285/52b08e7f-9fba-40a1-b0b5-dda9a3c83be2
2. Al-Khulaifi, Y., Lin, Q., Blunt, M.J., Bijeljic, B.: Pore-scale dissolution by CO_2 saturated brine in a multimineral carbonate at reservoir conditions: impact of physical and chemical heterogeneity. Water Resour. Res. **55**(4), 3171–3193 (2019)
3. Alizadeh, A.H., Akbarabadi, M., Barsotti, E., Piri, M., Fishman, N., Nagarajan, N.: Salt precipitation in ultratight porous media and its impact on pore connectivity and hydraulic conductivity. Water Resour. Res. **54**(4), 2768–2780 (2018)
4. Costa, T.B., Kennedy, K., Peszynska, M.: Hybrid three-scale model for evolving pore-scale geometries. Comput. Geosci. **22**(3), 925–950 (2018)
5. Dadda, A., et al.: Characterization of microstructural and physical properties changes in biocemented sand using 3D x-ray microtomography. Acta Geotech. **12**(5), 955–970 (2017). https://doi.org/10.1007/s11440-017-0578-5
6. Fedkiw, R.P., Aslam, T., Merriman, B., Osher, S.: A non-oscillatory Eulerian approach to interfaces in multimaterial flows (the ghost fluid method). J. Comput. Phys. **152**(2), 457–492 (1999)
7. Ghommem, M., Zhao, W., Dyer, S., Qiu, X., Brady, D.: Carbonate acidizing: modeling, analysis, and characterization of wormhole formation and propagation. J. Petrol. Sci. Eng. **131**, 18–33 (2015)
8. Gibou, F., Fedkiw, R., Osher, S.: A review of level-set methods and some recent applications. J. Comput. Phys. **353**, 82–109 (2018)
9. Johansen, H., Colella, P.: A cartesian grid embedded boundary method for Poisson's equation on irregular domains. J. Comput. Phys. **147**(1), 60–85 (1998)
10. Kang, Q., Chen, L., Valocchi, A.J., Viswanathan, H.S.: Pore-scale study of dissolution-induced changes in permeability and porosity of porous media. J. Hydrol. **517**, 1049–1055 (2014)

11. Kaya, E., Zarrouk, S.J.: Reinjection of greenhouse gases into geothermal reservoirs. Int. J. Greenhouse Gas Control **67**, 111–129 (2017)
12. Khachkova, T., Lisitsa, V., Reshetova, G., Tcheverda, V.: GPU-based algorithm for evaluating the electrical resistivity of digital rocks. Comput. Math. Appl. **82**, 200–211 (2021)
13. Lebedev, M., Zhang, Y., Sarmadivaleh, M., Barifcani, A., Al-Khdheeawi, E., Iglauer, S.: Carbon geosequestration in limestone: pore-scale dissolution and geomechanical weakening. Int. J. Greenhouse Gas Control **66**, 106–119 (2017)
14. Li, X., Huang, H., Meakin, P.: Level set simulation of coupled advection-diffusion and pore structure evolution due to mineral precipitation in porous media. Water Resour. Res. **44**(12), W12407 (2008)
15. Lisitsa, V., Bazaikin, Y., Khachkova, T.: Computational topology-based characterization of pore space changes due to chemical dissolution of rocks. Appl. Math. Model. **88**, 21–37 (2020). https://doi.org/10.1016/j.apm.2020.06.037
16. Luo, K., Zhuang, Z., Fan, J., Haugen, N.E.L.: A ghost-cell immersed boundary method for simulations of heat transfer in compressible flows under different boundary conditions. Int. J. Heat Mass Transf. **92**, 708–717 (2016)
17. Miller, K., Vanorio, T., Keehm, Y.: Evolution of permeability and microstructure of tight carbonates due to numerical simulation of calcite dissolution. J. Geophys. Res.: Solid Earth **122**(6), 4460–4474 (2017)
18. Molins, S., et al.: Pore-scale controls on calcite dissolution rates from flow-through laboratory and numerical experiments. Environ. Sci. Technol. **48**(13), 7453–7460 (2014)
19. Osher, S., Fedkiw, R.P.: Level set methods: an overview and some recent results. J. Comput. Phys. **169**(2), 463–502 (2001)
20. Peskin, C.S.: Flow patterns around heart valves: a numerical method. J. Comput. Phys. **10**, 252–271 (1972)
21. Prokhorov, D., Lisitsa, V., Bazaikin, Y.: Digital image reduction for the analysis of topological changes in the pore space of rock matrix. Comput. Geotech. **136**, 104171 (2021)
22. Sotiropoulos, F., Yang, X.: Immersed boundary methods for simulating fluid-structure interaction. Prog. Aerosp. Sci. **65**, 1–21 (2014)
23. Steefel, C.I., et al.: Reactive transport codes for subsurface environmental simulation. Comput. Geosci. **19**(3), 445–478 (2015)
24. Sussman, M., Fatemi, E.: An efficient, interface-preserving level set redistancing algorithm and its application to interfacial incompressible fluid flow. SIAM J. Sci. Comput. **20**(4), 1165–1191 (1999)
25. Xu, Z., Meakin, P.: Phase-field modeling of solute precipitation and dissolution. J. Chem. Phys. **129**(1), 014705 (2008)
26. Yoon, H., Valocchi, A.J., Werth, C.J., Dewers, T.: Pore-scale simulation of mixing-induced calcium carbonate precipitation and dissolution in a microfluidic pore network. Water Resour. Res. **48**(2), W02524 (2012)